Repairing High γ' Hot Section Gas Turbine Components Using Advanced Manufacturing

An examination of how laser-blown powder deposition can be used to repair high γ' IN-100 superalloy gas turbine components

BY N. SRIDHARAN, Y. LEE, B. JORDAN, J. ROBERTSON, AND R. RAMAKRISHNAN

Abstract

This article describes the ability to use laser-blown powder deposition to repair high γ' IN-100 superalloy gas turbine components. The influence of various process conditions on the ability to make crack-free IN-100 deposits over surrogate high γ' alloys was investigated to identify cracking mechanisms in the deposit and heat-affected zones (HAZs). The various crack formation mechanisms, such as solidification cracking and liquation cracking, were evaluated using multiscale characterization and numerical simulation. The cracking in the deposit region was predominantly solidification cracking, while those observed in the HAZ were liquation cracking. The results showed that controlling thermally induced residual stresses is the key to eliminating cracking, and the optimum preheat temperature was determined. The results were then contrasted with those in published literature and an approach to effectively repair hot section parts was presented.

Keywords

- Additive Manufacturing
- Cladding
- Ni Alloys
- Numerical Analysis
- Weldability

https://doi.org/10.29391/2023.102.023

Introduction

High γ' Ni-based superalloys are used in harsh operating conditions requiring high tensile strength, high creep strength, oxidation resistance, and fatigue strength (Ref. 1). To achieve through-life cost reduction targets, component refurbishment, overhaul, and repair are prime considerations for both original equipment manufacturers (OEMs) and operators (Refs. 1, 2). However, polycrystalline high γ' Ni-based superalloys also have poor weldability and are deemed nonweldable (Refs. 2, 3) because of various cracking mechanisms, including solidification (Refs. 4–6), liquation (Ref. 7), strain-age (Refs. 8, 9), and ductility-dip cracking (Refs. 8, 9) caused by complex thermal profile and mechanical constraints. Weldability in this context is defined as "the capacity of a material to be joined under the imposed fabrication conditions into a specific, suitably defined structure and to perform satisfactorily in the intended service with minimum defects and distortion" (Refs. 10, 11).

Ni-based superalloys are heavily alloyed with Al, Ti, B, Cr, Ta, W, Co, and Zr to optimize the size and shape of γ' and simultaneously improve grain boundary stability by inducing carbide and precipitates through heat treatment. Solute partitioning (due to alloying) widens the solidification temperature range. Increasing the solidification temperature range widens the semisolid region known as the mushy zone. It has been reported that the propensity of solidification cracking is directly proportional to the mushy zone. Solidification cracking occurs when the mushy zone experiences tensile stresses and a high fraction of solid (typically $0.7 < fs < 0.98$) restricts the flow of liquid metal to backfill the interdendritic regions during the solidification process (Refs. 10, 11). The liquid film present at the grain boundaries cannot accommodate the thermal stress and consequently leads to cracking along the grain boundaries (Refs. 1, 10). Grain boundary liquation (in the case of liquation cracking) occurs primarily due to the localized dissolution of the precipitates and grain boundary phases, such as carbides (Refs. 10, 12). Constitutional liquation was first coined by Pepe and Savage (Ref. 13). This

Table 1 — Composition of the Substrate and Powder Used in This Study

Alloy	W wt-%	Co wt-%	Cr wt-%	Al wt-%	Ta wt-%	Hf wt-%	Ti wt-%	Mo wt-%	C wt-%	Ni wt-%
Substrate	10.19	9.92	8.40	5.58	3.12	1.11	0.92	0.64	0.13	Bal.
IN-100	—	18.4	12.4	4.9	—	—	4.3	3.2	0.07	Bal.

mechanism involves at least two different phases (typically a precipitate matrix) that reach to form a liquid phase via a eutectic reaction during rapid heating. During rapid heating, the precipitate does not have time to dissolve and, at the eutectic temperature, liquates via a eutectic reaction (Refs. 12, 14). A liquid film forms that embrittles the grain boundaries and leads to cracking under the tensile thermal stresses that develop during the deposition process. Strain-age cracking, on the other hand, occurs during the postweld heat treatment stage (Ref. 1). These defects are characterized by intergranular microcracking as a result of precipitation hardening of the alloy, which increases the strength of the grain but consumes ductility. The strain-age cracking occurs when the precipitation hardening overlaps intrinsic and extrinsic strain (Ref. 15). The classical way to avoid this problem is either to solutionize the material or overage the material before welding (Refs. 16–18). This approach combined with using a more ductile filler material such as IN-625, and a careful design of postprocessing heat treatments, has shown to be an effective way to mitigate this cracking mechanism. In many cases, all these mechanisms operate simultaneously (Ref. 12). Typically, all alloys containing greater than 30–50% γ' have decreased weldability due to their high susceptibility of solidification cracking during welding and strain-age cracking during postweld heat treatment due to the precipitation of γ' (Refs. 1, 3).

In the past, some traditional repair techniques such as plasma spraying (Ref. 19), plasma transfer arc welding (Refs. 20, 21), and gas tungsten arc welding (Ref. 22) were adopted to repair high γ' alloys. These techniques have limited success and often suffer from large mushy zone formation, which leads to cracking in the welded layers. Arc-based welding processes often lead to heat-affected zone (HAZ) liquation cracking and solidification cracking in the fusion zone (FZ) (Refs. 1, 2, 7). Hence, it is important to develop repair processes that minimize the mushy zone and HAZ formation (Refs. 2, 23). Recently, laser metal deposition/laser cladding techniques have been used to repair weld materials (Refs. 7, 24, 25). The laser beam melts a thin layer of the substrate (part to be repaired), and powder is injected into the weld pool, resulting in a metallurgically bonded deposit with minimum liquation (Refs. 26, 27). The key advantage is the significantly smaller HAZ and mushy zone, which leads to a decrease in the cracking susceptibility.

Despite these benefits, depositing high γ' alloys remains challenging due to various cracking mechanisms. To overcome this, most of the repairs done today entail depositing a ductile filler material (such as IN-625) in the low-stress region of the part (Refs. 1, 2). Rarely have attempts been performed to repair these structures with a matching filler material. Acharya et al. (Ref. 3) used scanning laser epitaxy and performed a full factorial design of experiments (DOE) to optimize the number of preheat scans to ensure a fully sound deposit. The results showed that deposits fabricated with a volumetric energy density between 20–30 J/mm^3 and 80–120 preheat passes produced acceptable deposits without any cracks. The preheat passes served to reduce the thermal gradient and the extent of tensile residual stresses in the parts (Ref. 3).

A similar concept was used to repair IN-738 where induction-assisted laser cladding was used (Ref. 28). The authors observed that when the preheating exceeded 800°C (1472°F), a crack-free deposit could be obtained. A similar study was performed where the role of preheat on the ability to fabricate IN-738LC via laser forming was investigated. The authors documented that a progressive increase in the preheat temperature resulted in a steady decrease in the crack length. Specifically, the crack length dropped from 60 to 10 mm (2.362 to 0.394 in.) when the preheat was increased from room temperature to 800°C. To obtain a crack-free deposit, a preheat of 1050°C (1922°F) was necessary. This increase in preheat temperature resulted in a sharp decrease in the thermal gradient from 1.7×10^6 K/m (room temperature) to 1.1×10^6 K/m (800°C) to 6.5×105 K/m (1050°C) (Ref. 29). This is different from the results reported by Chinag and Chen (Ref. 28) where crack-free deposits could be obtained at a preheat of 800°C, which is lower than the 1050°C reported by Xu et al. (Ref. 29). This could be an effect of the difference in part geometries between the two studies. Changes in part geometry could alter the thermomechanical response during fabrication, leading to cracking in Ni-based superalloys. Considering the importance of geometries, which determine the cracking susceptibility, this study was devoted to understanding and mitigating FZ and HAZ cracking in IN-100 repair welds made on mock-up test plates simulating the actual repair conditions. This investigation demonstrated the feasibility of depositing a 35 × 15 × 5-mm (1.378 × 0.591 × 0.197-in.) IN-100 on a surrogate substrate with representative geometries of the actual parts.

Experimental Procedure

Deposit Fabrication and Characterization

The composition of the substrate material and the powder material used are shown in Table 1. The IN-100 powder was gas atomized with a particle size distribution of 40–120 μm in diameter. The hall flow rate of the powder was 19 s. The substrate was a mock-up piece of MAR-M-247 that was

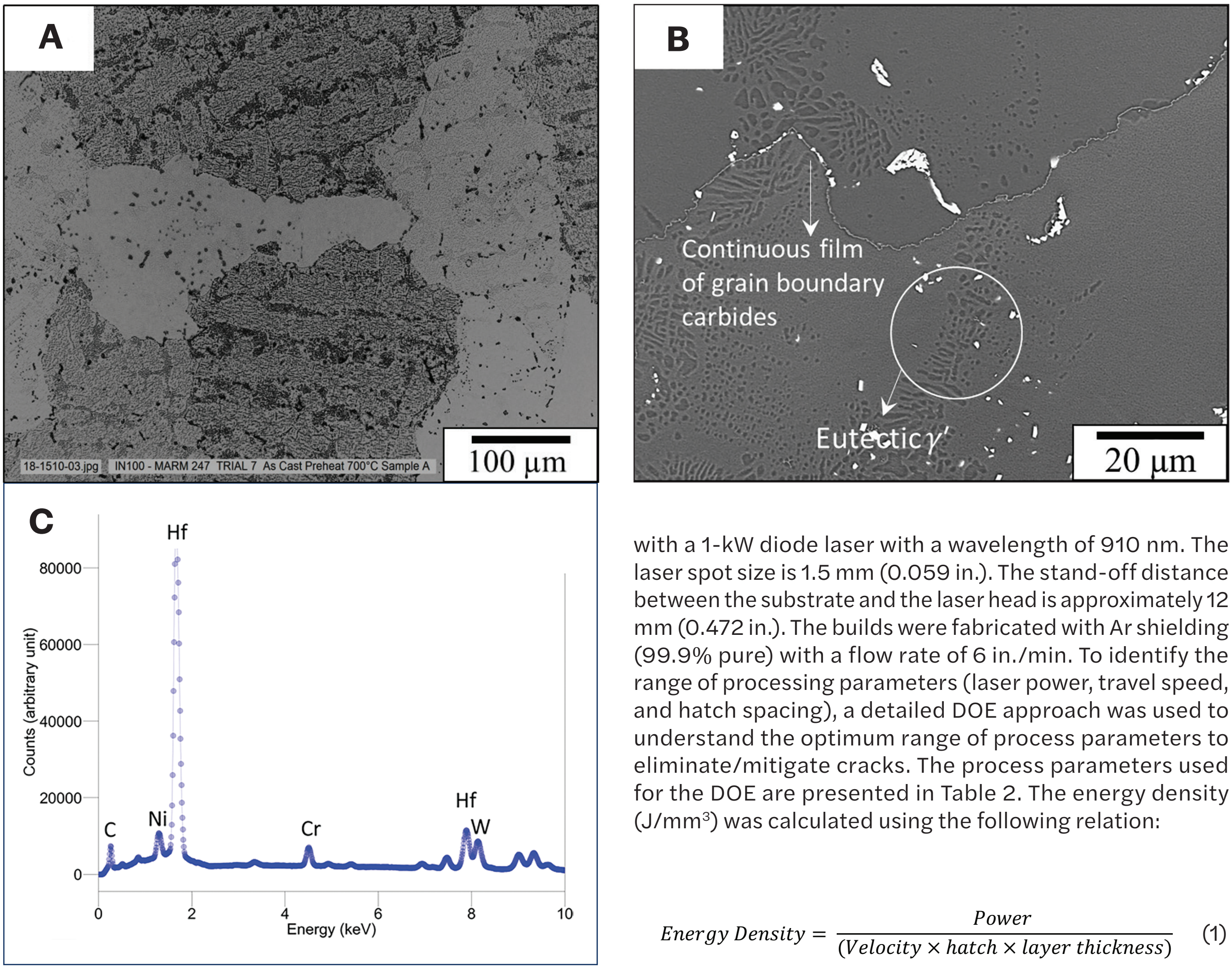

Fig. 1 — A — Optical micrograph of the as-cast substrate; B — SEM backscatter image of the substrate showing the presence of eutectic γ′ and a continuous string of carbides along the grain boundaries; C — EDS spectrum showing the brighter particles at grain boundaries were probably Hf-rich MC-carbides.

used in the as-cast and solution-annealed condition (1093°C [1999°F] for 2 h in a vacuum furnace) to evaluate the role of initial microstructure on cracking susceptibility of the builds. MAR-M-247 was used due to the nonavailability of IN-100 substrates and because it is similar in chemistry and physical metallurgy to IN-100. The chemical compositions are described in Table 1.

Directed energy deposition (DED), a laser powder-blown additive manufacturing (AM) technique, was used for deposition/repair trials. This process utilizes a laser focused on a substrate material, creating a weld pool into which powder is sprayed coaxially or via an off-axis technique to deposit material. The laser head then rasters in the X-Y plane at a programmed velocity and the entire assembly moves up in the Z direction once the layer is complete. The DM3D 103D system located at the Oak Ridge National Laboratory Manufacturing Demonstration Facility, Knoxville, Tenn., is equipped with a 1-kW diode laser with a wavelength of 910 nm. The laser spot size is 1.5 mm (0.059 in.). The stand-off distance between the substrate and the laser head is approximately 12 mm (0.472 in.). The builds were fabricated with Ar shielding (99.9% pure) with a flow rate of 6 in./min. To identify the range of processing parameters (laser power, travel speed, and hatch spacing), a detailed DOE approach was used to understand the optimum range of process parameters to eliminate/mitigate cracks. The process parameters used for the DOE are presented in Table 2. The energy density (J/mm^3) was calculated using the following relation:

$$Energy\ Density = \frac{Power}{(Velocity \times hatch \times layer\ thickness)} \tag{1}$$

The same parameters were used to make deposits on both the as-cast and the solution-annealed substrates. All the builds were sectioned using conductive Bakelite and polished using standard metallographic techniques. Following polishing, the samples were etched using Kallings reagent to reveal the structure. Optical microscopy on the samples was performed using a Zeiss optical microscope. Scanning electron microscopy (SEM) was performed using a JEOL 6500F equipped with energy dispersive spectroscopy (EDS) and electron backscattered diffraction (EBSD) detectors. Imaging was performed using a voltage of 20 kV and a probe current of 4 nA using both a secondary electron detector and a backscatter electron detector.

Simulation Methodology

AM involves widely varying thermal signatures that lead to complex interactions between process parameters, part geometry, and spatial and temporal variations of cracking susceptibility. It is important to know the correlation between process parameters, including preheating, temperature distribution, and stress evolution, during the printing process over all positions on the layer. The simulations were

Table 2 — Process Parameters Used to Evaluate Cracking Susceptibility in the Builds

	Laser Power (W)	Travel Speed (mm/min)	Hatch Spacing (mm)	Powder Feed Rate (gram/min)	Energy Density (J/mm^3)
Trial 1	400	800	0.6	4	100
Trial 2	400	1000	0.6	4	80
Trial 3	400	800	0.5	4	120
Trial 4	600	800	0.6	4	150
Trial 5	600	1000	0.6	4	120
Trial 6	600	1000	0.5	4	144

performed to understand the effects of welding parameters on the cracking tendency of the material and to optimize the preheat temperature. A finite element method code, ABAQUS (Ref. 30), was used for thermal and stress analysis. The temperature increase of powder particles during flight was assumed to be a constant of 1100°C (2012°F). The effect of fluid flow on temperature and melt pool shape was neglected. The dimensions of the deposit were 20 × 15 × 0.5 mm (0.787 × 0.591 × 0.020 in.) and the substrate was 25 × 20 × 2 mm (0.984 × 0.787 × 0.079 in.). The model had 8-node hexahedron elements for heat transfer (DC3D8) and stress (C3D8) analysis. The mesh size of 0.1 (0.004 in.) and 1 mm (0.039 in.) was used for the deposit and substrate, respectively. The moving laser beam was modeled as a Gaussian double-ellipsoidal heat source model (Ref. 30). The mathematical equation of the heat source is expressed by Equation 2.

$$\dot{Q}(x,y,z,t) = \frac{2\eta P}{abc\pi\sqrt{\pi}} \exp\left(-\frac{(x+v_x t)^2}{a} + \frac{y^2}{b} + \frac{z^2}{c}\right) \qquad (2)$$

where Q is heat flux; η is the absorptance; P is the arc power; v_x is the velocity of moving the heat source; and a, b, and c are the dimensions of the heat source along the x, y, and z axes, respectively. Furthermore, the heat loss by convection and radiation through the surrounding environment is considered as a combined heat transfer coefficient. The equation (Ref. 30) is given below:

$$h_{loss} = \varepsilon \cdot 24.1 \times 10^{-4} \cdot T^{1.61} \qquad (3)$$

where h_{loss} is the combined heat transfer coefficient, ε is emissivity, and T is the temperature.

Results and Discussions

Deposits on the As-Cast Substrate

The substrate was characterized using optical microscopy and SEM. Results are shown in Fig. 1. Figures 1A–C show the optical and SEM micrographs of the substrate samples in the as-received conditions. The microstructure of the as-cast substrate showed three major constituents: the γ matrix, primary γ', and eutectic γ' along with grain boundary carbides. The eutectic γ' was differentiated from the precipitates by the large irregular-shaped particles, as shown in Fig. 1C. Eutectic γ' typically forms due to the aggressive partitioning of Al and Ti to the liquid during solidification (Refs. 8, 31). In addition to the presence of γ', the grain boundaries were decorated by Hf/Ta-rich carbides as shown in Fig. 1B. Minor additions of Hf, B, and C tend to result in the formation of carbides often located along the grain boundaries directly from the liquid state at the terminal end of solidification (Refs. 31–33). EDS analysis showed the carbides were predominantly Hf-rich MC carbides.

The macrographs of the samples fabricated in the as-deposited condition are presented in Figs. 2A–F. The arrow shows the direction of laser beam travel. The arrowhead points to the end while the other side indicates the beginning of the deposit. In all the samples, the cracking was more pronounced during the start of the deposit and the intensity of cracking reduced toward the end of the deposit. In addition, for all the samples, nearly 70% of the cracks initiated in the substrate and propagated into the deposit. Among all the deposits fabricated, Fig. 2F showed the best results (least cracking) were obtained for deposits fabricated using a tighter hatch spacing. In the case of samples 2D and F, there was a transition of 14 mm (0.551 in.) from the deposit start where the cracking did not occur. These samples were fabricated with an energy density greater than 120 J/mm^3 and were more resistant to cracking. Figures 3A–D show the interface of the deposits fabricated on the as-cast substrate. Figures 3A and B show cracking occurred at the start of the deposit. Cracks were also observed in the deposit. The etched micrographs

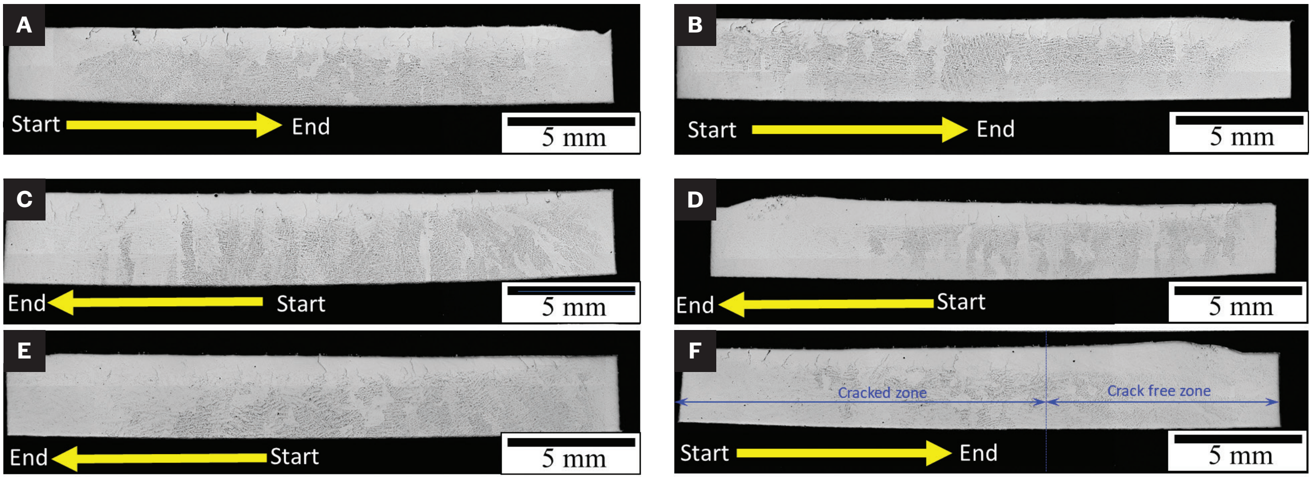

Fig. 2 — Optical macrographs of the simulated repairs done using various process parameters: A — Laser power 400 W, travel speed 800 mm (31.496 in.)/min, hatch spacing of 0.6 mm (0.024 in.); B — laser power 400 W, travel speed 1000 mm (39.370 in.)/min, hatch spacing of 0.6 mm; C — laser power 400 W, travel speed 800 mm/min, hatch spacing of 0.5 mm (0.020 in.); D — laser power 600 W, travel speed 800 mm/min, hatch spacing of 0.6 mm; E — laser power 600 W, travel speed 1000 mm/min, hatch spacing of 0.6 mm; F — laser power 600 W, travel speed 1000 mm/min, hatch spacing of 0.5 mm.

also show that the cracks in the HAZ were predominantly intergranular in nature along the continuous string of grain boundary carbides. In certain cases, these cracks extended into the deposit, while in other cases the cracks nucleated in the deposit. The cracks in the deposit seemed to show a significant amount of eutectic, indicating that the cracks were predominantly hot cracks. Cracking occurs when the accumulated tensile stresses exceed a set threshold and there is a nonavailability of enough liquid to heal cracks. The tensile stresses were significantly higher at the start of the deposit (on a cold substrate). Toward the end of the deposit, the preheating effect from the previous passes served to reduce the tensile stresses during solidification, thus reducing the cracking tendency. A more detailed explanation will be presented in the discussions section of this paper. The same explanation could also explain the reduced cracking when welding with a tighter hatch spacing. The overall temperature of the base plate increased and acted as a preheat with the effect of lowering the overall tensile stresses.

To ascertain the operating cracking mechanisms, a more detailed investigation using SEM was performed. The results from the SEM are presented in Fig. 3C. The SEM showed clear evidence of cracking along the carbides in the HAZ. The carbides were identified to be rich in Hf and Ti, as shown in the EDS spot analysis. The EDS spectrum of the liquated carbides near the cracks did not show any significant deviation from the carbides observed in the as-cast virgin material. Note that in several locations the cracks initiated in the HAZ and propagated into the deposit.

While there are significant carbides that form due to the Liquid → MC (Hf/Ta) + γ eutectic reaction, during the solidification the cracking does not occur due to the liquation of these carbides. However, the presence of solute-rich eutectic films along the crack boundaries could be indicative of solidification cracking as detailed in literature (Ref. 8). An analysis of the cracks in the deposited material and the HAZ indicates that most of the cracks were intergranular as well, as shown by the EBSD micrographs in Figs. 4A and B. This mechanism is characteristic of liquation (Refs. 4, 6, 7), and solidification cracking and has been documented in the existing literature (Ref. 7). In addition, high-magnification EBSD scans in regions adjacent to the HAZ cracks showed tell-tale signs of accumulated plastic deformation followed by recrystallization (Refs. 34–36) in the regions adjacent to the cracks, as shown in Fig. 4B. The presence of recrystallized grains indicates that the cracking occurred at recrystallization temperatures, which is typically above the liquating temperature of the grain boundary carbides.

Deposits on Solution-Annealed Coupons

Characterization of the deposits fabricated on an as-cast substrate showed a strong correlation to the cracking susceptibility in the HAZ and the presence of grain boundary carbides. It has been documented previously that these carbides in the interface liquate, leading to cracks spreading from the HAZ into the deposit (Ref. 7). Examination of the deposits shown in Fig. 2 also showed that more than 70% of the cracks originated from the substrate. Constitutional liquation can occur due to the presence of a continuous string of grain boundary carbides (Ref. 7) and the eutectic γ' (Refs. 6, 37, 38). Since the majority of the cracks existed in the HAZ in all the builds fabricated, it was hypothesized that breaking the continuous network of grain boundary carbides and the eutectic γ' would reduce the cracking susceptibility.

Previous reports showed that the solution annealing at 1250°C (2282°F) resulted in a carbide-free microstructure and eliminated eutectic γ' (Ref. 13). However, 1250°C also increases the risk of liquation, considering the temperature is very close to the equilibrium solidus temperature of the alloy, approximately 1281°C (2338°F) (Ref. 14). To ensure that the liquation did not occur, solution annealing was performed at

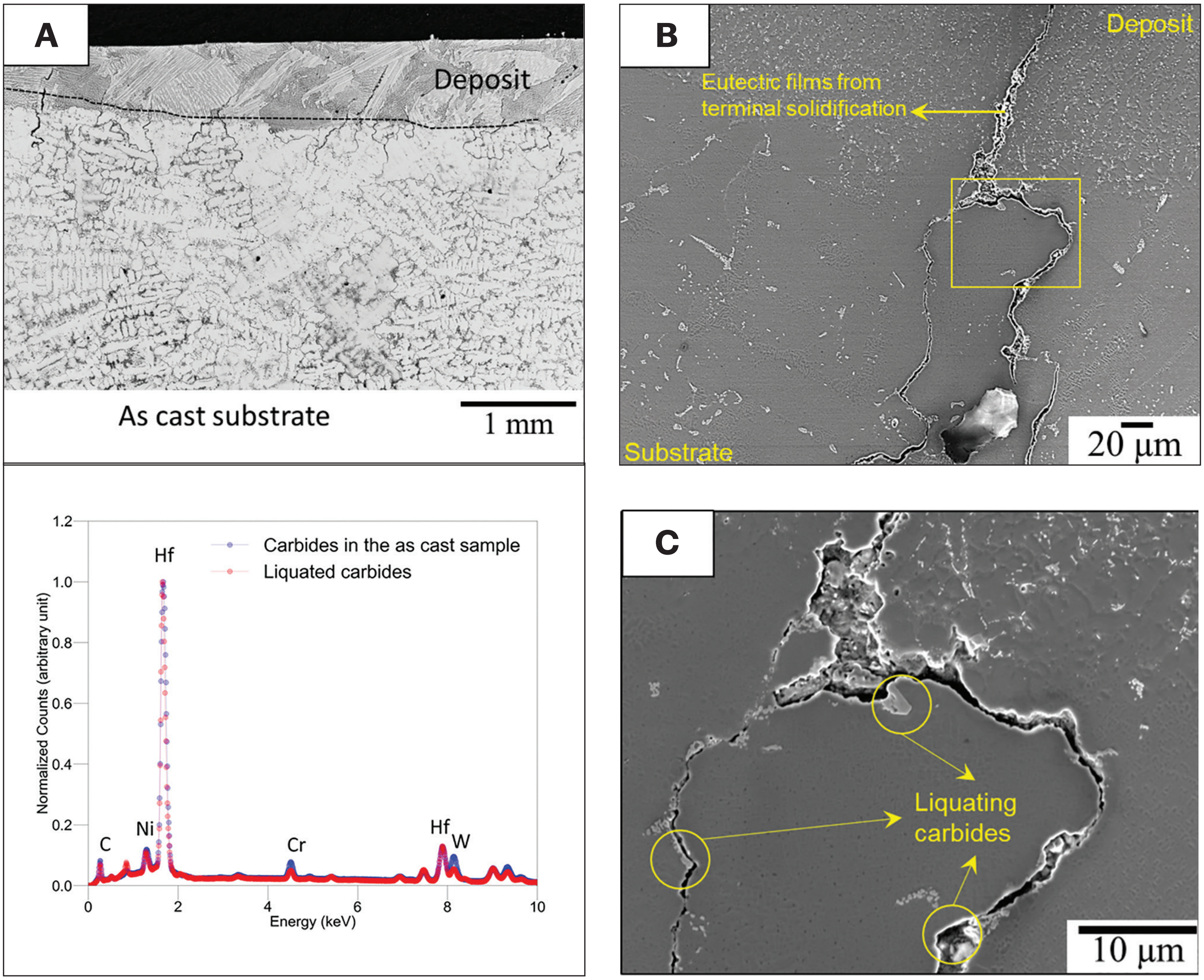

Fig. 3 — Micrographs of the cracked locations of the deposits: A — Optical micrograph showing that the cracks occurred in both the HAZ and deposit material; B — SEM micrograph showing the presence of eutectic films along the cracks in the deposit; C — SEM micrograph showing the presence of cracking in the interface near the MC carbides (shown in the inset EDS spectrum).

1100°C for 2 h. Previous work showed that solution annealing at this temperature was an effective strategy and reduced the fraction of eutectic from almost 20% to less than 10%. In addition, the treatment was also effective in breaking down the continuous network of grain boundary carbides (Ref. 39). Therefore, to eliminate the carbides, a standard solution annealing treatment (1100 ± 10°C [50°F]/2h in Ar) was given to the substrates.

The solution-annealed substrates are also shown in Figs. 5A–C. Solution annealing led to the breakdown of the continuous network of carbides along the grain boundary. While the grain boundary carbides dissolved, EDS showed that the actual composition of the Hf-rich carbides did not change significantly after the heat treatment. In addition, the procedure coarsened the secondary γ′ precipitates and reduced the fraction of eutectic γ′ as reported elsewhere (Refs. 39, 40). Previous reports have shown that solution annealing the substrates before repairing resulted in improved resistance to cracking (Ref. 1). Figures 5A and B clearly show that solution annealing plates eliminated the continuous grain boundary carbides and coarsened the fine secondary γ′ precipitates in the as-received material.

Based on the previous trials, it was concluded that the best results in terms of reduction of cracking density were obtained using parameter set number 6, shown in Table 2. The optical micrographs of the fabricated samples are shown in Fig. 6. Figure 6 shows that while solution annealing did not eliminate cracking, the cracking tendency was reduced by approximately 30%. This can be attributed to the elimination of the continuous network of grain boundary carbides as a result of the solutionizing annealing treatment. Detailed SEM investigations were performed to identify the cracking mechanisms. The micrographs are shown in Figs. 7A–C. The SEM micrographs show that similar cracking mechanisms operated despite the solution annealing treatments being performed. The HAZ cracking persisted and occurred

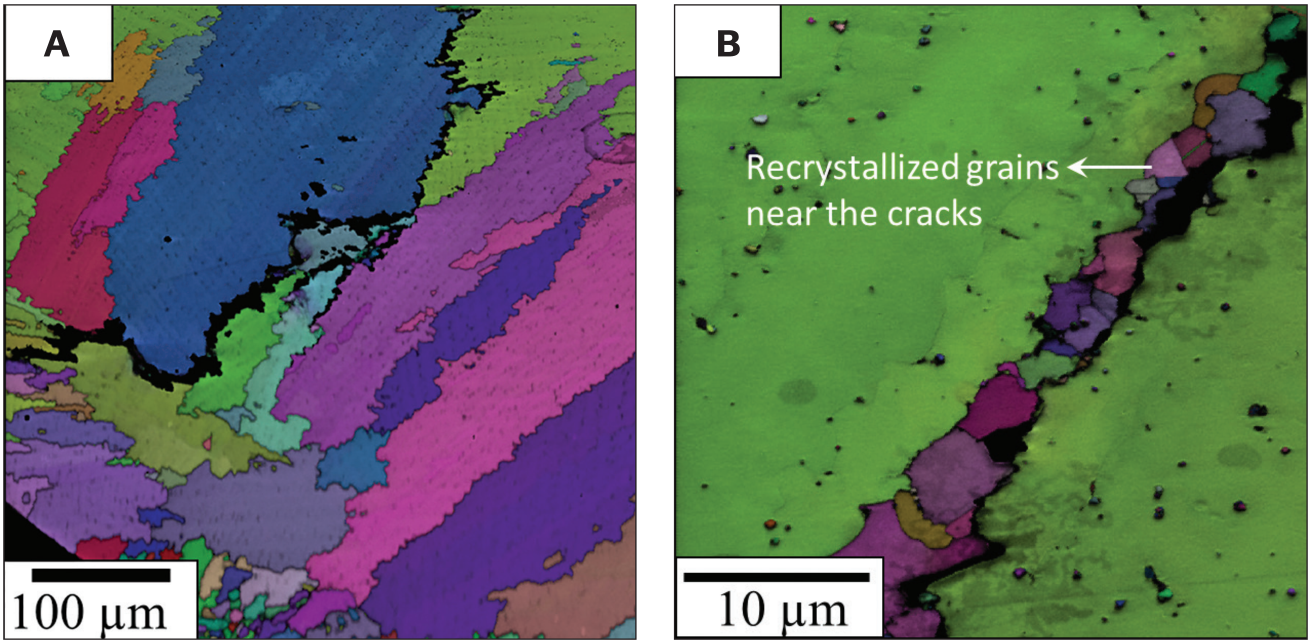

Fig. 4 — EBSD inverse pole figure maps: A — Deposit showing the presence of intergranular solidification cracks along the grain boundaries; B — cracks in the HAZ. Note the presence of fine equiaxed grains (indicating dynamic recrystallization) adjacent to the cracks, which indicate extensive plastic deformation at elevated temperatures.

Table 3 — Number of Cracks Detected in the Builds

Power (W)	Travel Speed (mm/min)	Hatch Spacing (mm)	Solidification Cracks	Liquation Cracks	Total Cracks
400	800	0.6	32	24	56
400	1000	0.6	31	14	45
400	800	0.5	36	30	66
600	800	0.6	30	25	55
600	1000	0.6	15	25	40
600	1000	0.5	15	18	33

adjacent to the carbide phases, which liquated as shown in Fig. 7B. In this case, the cracks in the IN-100 deposits were predominantly attributed to solidification cracking, as shown in Fig. 7A. While solution annealing reduced the cracking susceptibility in the builds, it was not possible for solution annealing to eliminate cracking in the deposits.

Rationalization of Cracking Mechanisms

To mitigate cracking in the deposits, it is important to understand the mechanisms of cracking in the builds. Based on the observations, two dominant cracking mechanisms were observed, viz., solidification cracking and constitutional liquation cracking.

Liquation cracking predominantly occurred in the substrate adjacent to carbides, and solidification cracking occurred in the deposited material. Both cracking mechanisms involve the formation of liquid films along the grain boundaries, which leads to cracking. The cracks could be classified into solidification and liquation cracks, respectively, based on morphology. Therefore, to unravel the cracking mechanisms, the number of cracks in each sample was imaged and counted, and the results are presented in Table 3. The same results are illustrated graphically in Figs. 8A and B, where the relationships between the number of cracks (both solidification cracks and liquation cracks) and

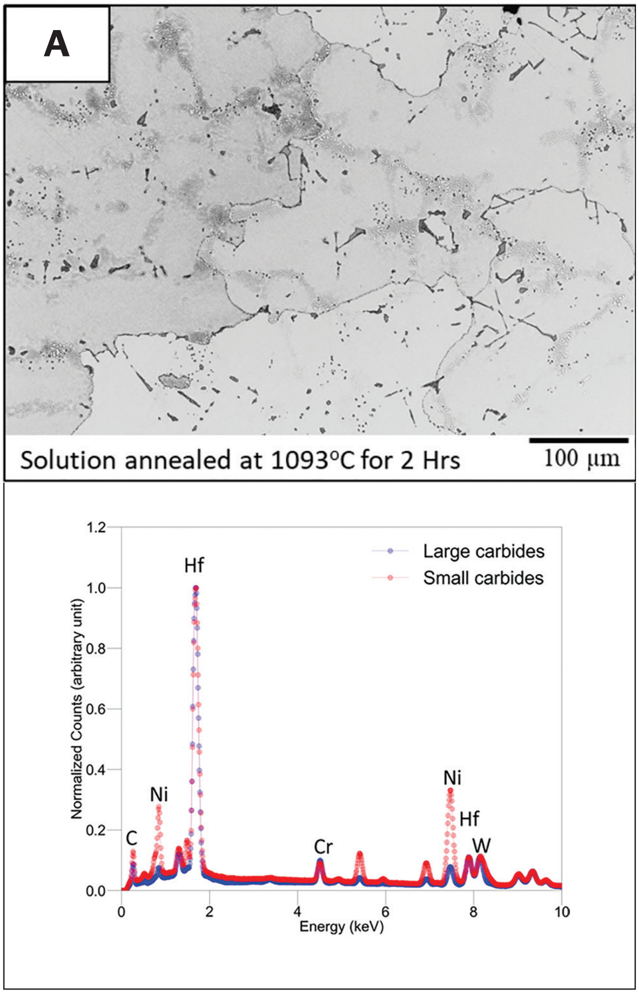

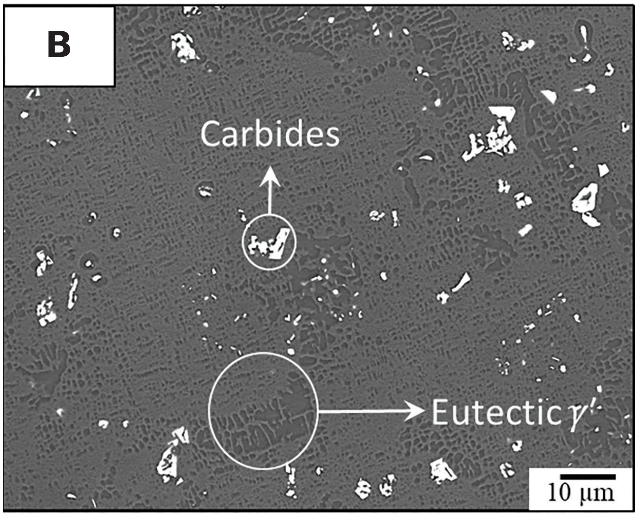

Fig. 5 — Micrographs of the solution-annealed plates: A — Optical microscopy; B — SEM micrograph displaying the breakdown of the grain boundary carbides and the associated EDS spectrum of the carbides, which shows that the carbides after solution annealing are Hf-rich carbides.

the various process parameters (laser power, travel speed, and hatch spacing) are presented. The plot displaying the velocity and travel speed shows a significant reduction in both solidification and liquation cracks for an increase in the travel speed. For the same laser power, the samples fabricated with a higher travel speed greatly reduced the susceptibility to solidification cracking. However, no such trends could be observed in the case of liquation cracking in the HAZ. These results were in sharp contrast to those obtained by Ref. 41, where the authors observed a reduction in liquation cracks by decreasing the laser power.

Therefore, to rationalize these differences with published literature, a more detailed understanding of the cracking mechanisms is warranted.

Solidification Cracking

Solidification cracking is typically restricted to the semi-solid mushy zone. The mushy zone typically consists of three distinct regions: 1) easy liquid feeding up to a solid volume fraction, 2) restricted liquid feeding ($0.7 < fs < 0.98$), and 3) no liquid feeding. The two-phase zone during solidification experiences tensile stresses due to the shrinkage stresses, which if exceeded beyond a threshold are sufficient to cause cracking along the dendrite arms (Ref. 42). When the volume fraction of the solid is very high and the opening cannot be healed by the backflow of liquid (region 2 and 3), the tears occur and propagate with further stresses. This cracking mechanism is promoted by a wide solidification range and welding at low travel speed (Ref. 22). Welding at low speeds promotes the generation of tensile stresses transverse to the trailing edge along the edge of the weld due to the contraction of the adjacent material. With progressive increases in travel speed, the material on either side of the weld trailing edge is being heated and therefore continuing to expand, thus generating compressive stresses (in the transverse direction), which suppress cracking. In this case, the samples that showed the highest resistance to solidification cracking were the samples fabricated with a travel speed of 1000 mm (39.370 in.)/min, the highest speed. In addition, the samples fabricated with a high travel speed showed that more than 85% of the cracks initiated in the substrate and propagated into the deposit, leading to cracking.

Liquation Cracking

Liquation cracking, or grain boundary fissuring, occurs predominantly in the HAZ. The metallurgical basis for HAZ grain boundary fissuring in Ni-based superalloys has been attributed to the persistence of liquid film in the grain boundary during the welding cycle (Ref. 43). It has been documented that the presence of grain boundary phases such as carbides, borides, and γ' could locally dissolve during the welding thermal cycle. This local dissolution has been observed in alloys such as IN-738, MAR-M-247, and Waspalloy (Refs. 10, 44). Rapid heating above the solidus temperature allows only for partial dissolution of the carbides (due to sluggish kinetic effects), leading to the formation of low-melting eutectic constituents. Typically, MC carbides liquate between 1225°–1245°C (2237°–2273°F) (Ref. 43). These liquated

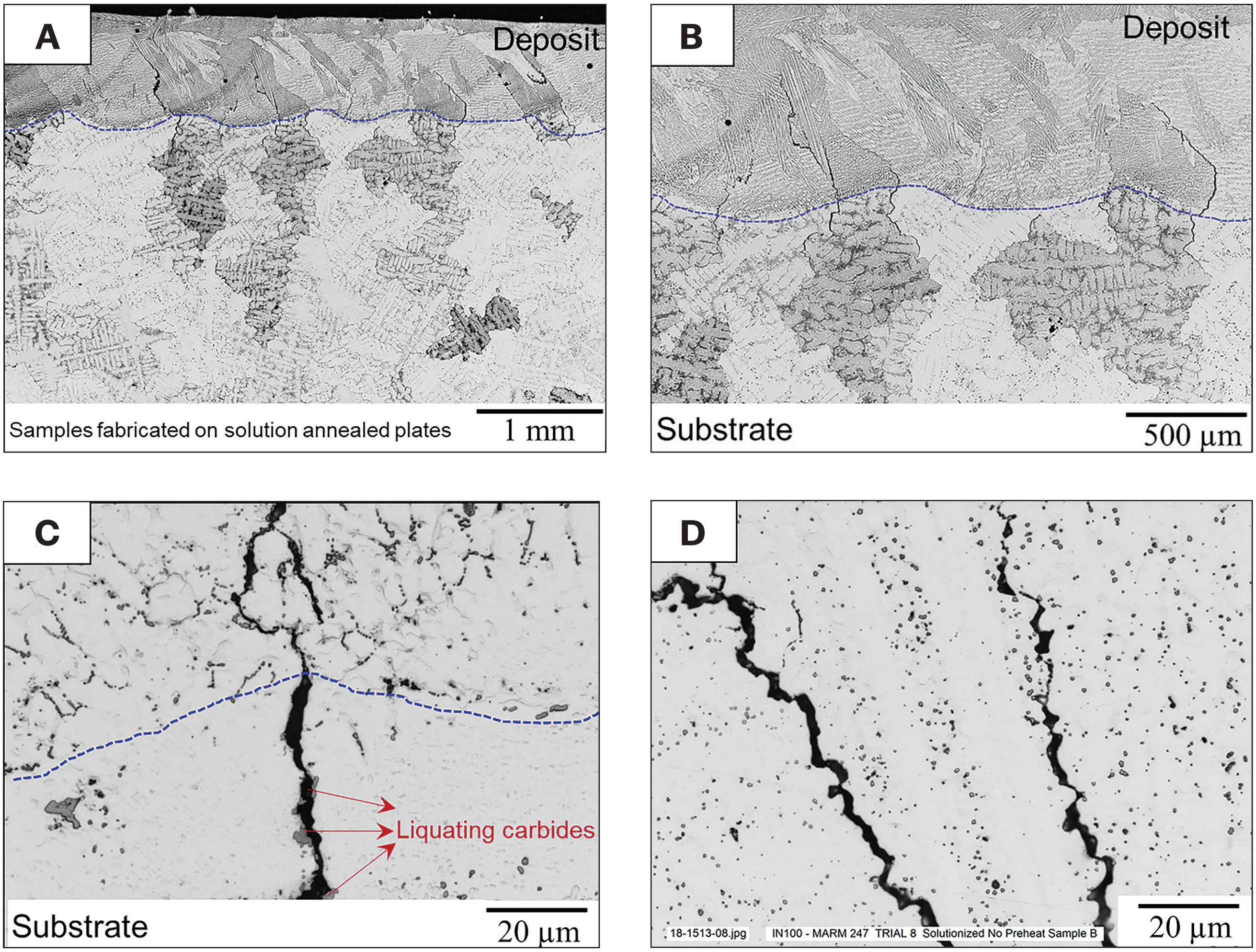

Fig. 6 — Optical micrographs of deposits fabricated on solution-annealed plates show that cracking persisted in locations adjacent to the carbides that liquated. Optical micrographs at: A — 50×; B — 100×; C — 500× showing the presence of liquating carbides in the base material; D — cracking along grain boundaries in the deposit.

films wet the grain boundaries, which are therefore unable to accommodate the thermal shrinkage stresses during cooling, leading to microfissuring.

Typically, high γ' Ni alloys lose their ductility on heating at a temperature called the nil ductility temperature (NDT). This temperature has been estimated to be close to 1160°C (2120°F) (Ref. 43). The range of temperature between the NDT and liquidus temperature is called the zero ductility temperature range (ZDTR). For the concerned alloy, this range is approximately 172°C (341.6°F) (Ref. 43), which is higher compared to austenitic stainless steel 310 (ZDTR approximately 61°C [141.8°F] [Ref. 45]) and solid solution-strengthened Ni alloys such as IN-625 (ZDTR 102°C [215.6°F][Ref. 45]). During cooling, the ductility is restored at a temperature indicated by the ductility recovery temperature (DRT), which is 970°C (1778°F). The difference between the on-heating peak temperature and the DRT is usually referred to as the brittle temperature region (BTR). The BTR is an indication of the period (per cooling rate) during which the ductility of the particular HAZ region experiencing the peak temperature within the ZDTR remains negligible upon cooling. In short, when the peak temperature exceeds the NDT, the on-cooling ductility is lower than the on-heating ones due to the grain boundary liquation delaying the ductility recovery. Therefore, the BTR is the most important indicator for crack susceptibility since the tensile strains that cause cracking do not set in until the weld starts to cool. The larger the BTR, the higher the propensity for cracking. The BTR for precipitation-strengthened alloys is typically 275°C (527°F) for a peak temperature of approximately 1245°C.

Solidification and liquation cracking in Ni-based superalloys, which is the dominant cracking mechanism in this case, has been attributed to the presence of a liquid film and shrinkage stresses arising from thermal strains (Refs. 10, 11).

Also, considering that most of the cracks nucleated in the HAZ and then proceeded to the deposit, the elimination of cracking in the HAZ was critical. Since characterization showed that the cracking in the HAZ was predominantly liquation cracking, it was necessary to eliminate liquation cracking.

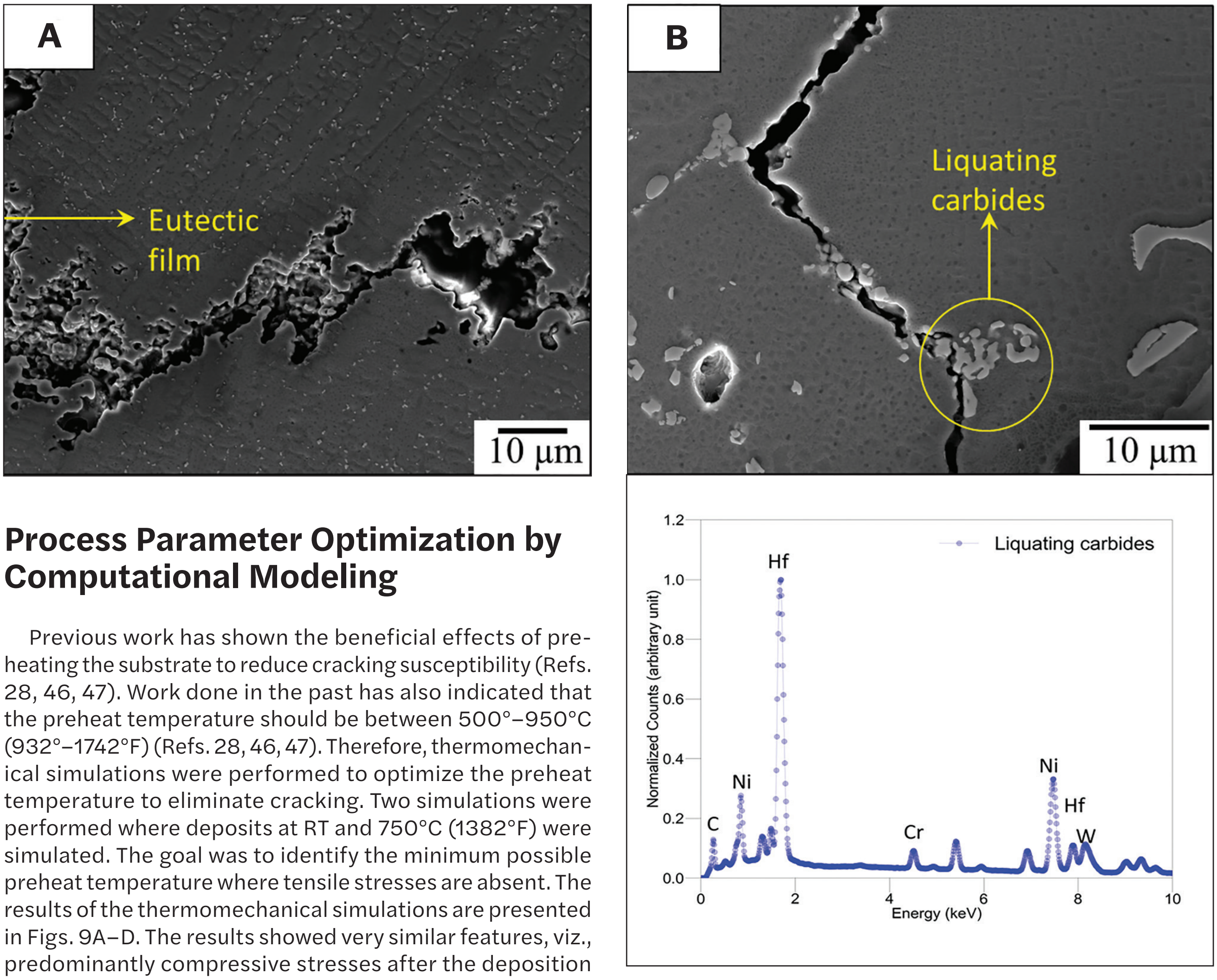

Fig. 7 — SEM micrographs showing the presence of: A — Eutectic films in the deposit region confirming the presence of solidification cracking; B — cracks propagating along the liquating carbides and the EDS spectrum confirming the same.

Process Parameter Optimization by Computational Modeling

Previous work has shown the beneficial effects of preheating the substrate to reduce cracking susceptibility (Refs. 28, 46, 47). Work done in the past has also indicated that the preheat temperature should be between 500°–950°C (932°–1742°F) (Refs. 28, 46, 47). Therefore, thermomechanical simulations were performed to optimize the preheat temperature to eliminate cracking. Two simulations were performed where deposits at RT and 750°C (1382°F) were simulated. The goal was to identify the minimum possible preheat temperature where tensile stresses are absent. The results of the thermomechanical simulations are presented in Figs. 9A–D. The results showed very similar features, viz., predominantly compressive stresses after the deposition was complete. However, the stresses after cooling transformed to tensile stresses. Also, note that the peak tensile stresses for the samples deposited at RT were significantly higher compared to those deposited at 750°C. As described in the previous section, the major factors that need to be considered are the NDT (temperature above which crack-free deformation is not possible) and the BTR, where the sample is susceptible to extensive cracking under tensile stresses. To rationalize the mechanisms of cracking in these deposits, the temporal changes to the stresses and temperature were extracted from identical locations for the samples fabricated at RT and 750°C. The location from which the data was extracted is shown in Fig. 10E and marked with a red dot. The dotted black line shows the location where the samples were sectioned for optical microscopy. As discussed previously, the samples showed extensive cracking only for the first approximately 20 mm, and the last 10 mm were crack free. Therefore, it is important to understand the thermomechanical evolution in these regions of the samples. The results are shown in Figs. 10A–D. The data shows the presence of a zone with a very high compressive stress field around the FZ ahead of the weld zone. The peak compressive stress in the samples fabricated at RT was approximately 300 MPa, and those fabricated with a preheat of 750°C also had a similar peak compressive stress. However, during cooling, after approximately 600 s, the samples fabricated at RT had a peak tensile stress of approximately 150 MPa, while the sample fabricated with a preheat of 750°C did not show the presence of tensile residual stress even after 600 s cooling. On a closer look, the BTR range was marked on the samples, and the results are presented in Figs. 10B and D. The data shows that all along the BTR crossing, the stresses in the samples fabricated at RT are tensile (approximately 50–80 MPa). While this may not be a significant tensile stress, the temperature at which this occurs was close to 1200°C (2192°F). It has been reported that γ' typically liquates at 1150°C (2102°F), and the MC carbides liquate between 1225–1245°C. In the presence of liquid films, the critical stress required to initiate cracking is given by (Ref. 9) the following:

$$\sigma = \frac{2\gamma_{SL}}{h} \qquad (4)$$

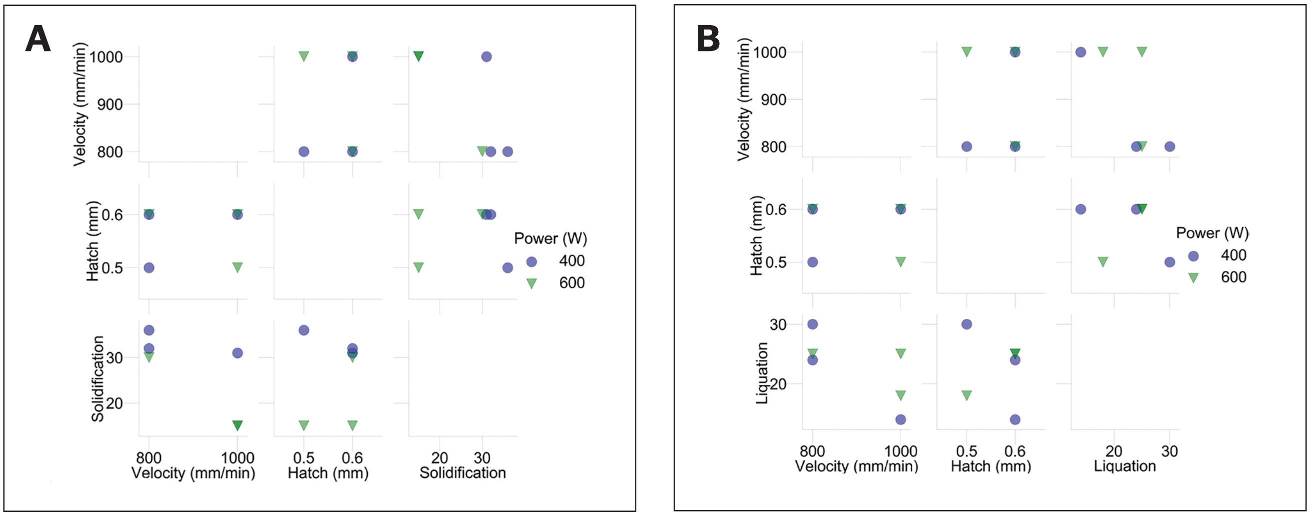

Fig. 8 — Pair plots showing the relationship between the laser power, travel speed, hatch spacing, and number of cracks in the deposit and HAZ.

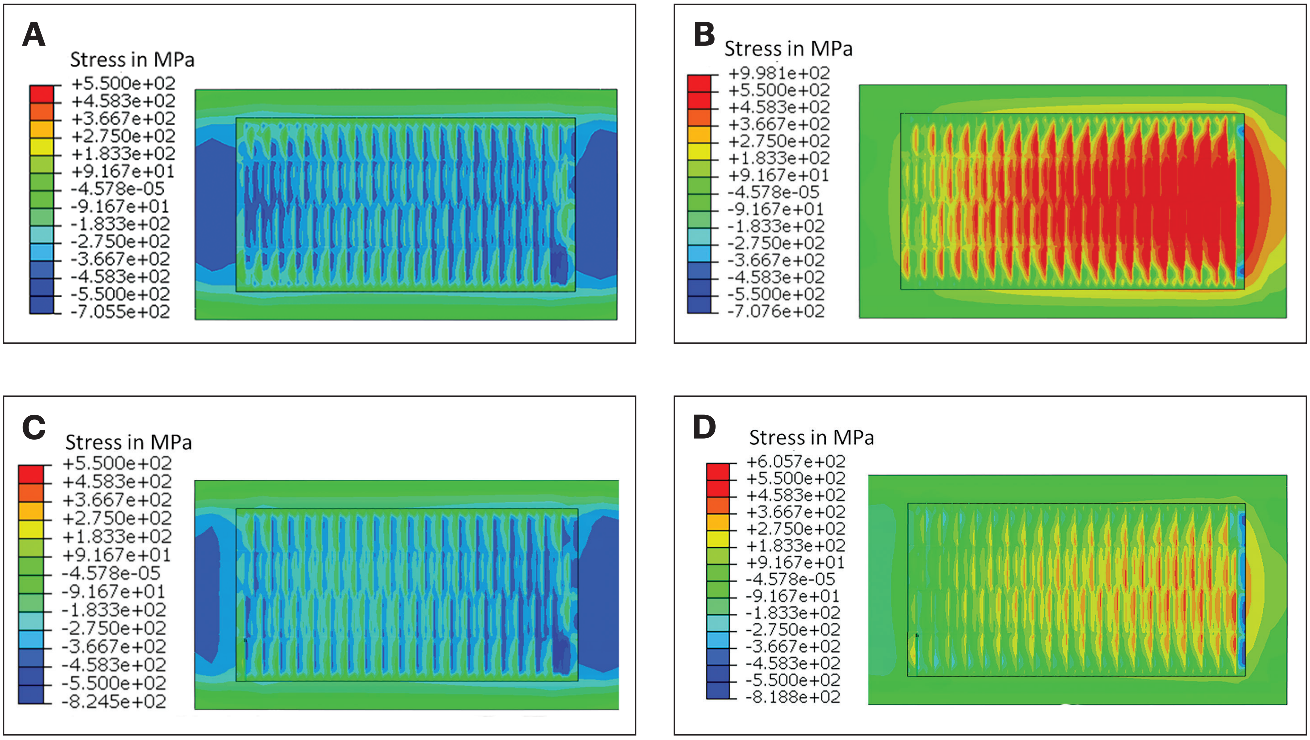

Fig. 9 — Results from the thermomechanical simulations of the simulated repair: A — Stress evolution on the simulated repair at room temperature immediately after the completion of the deposit; B — stress evolution on the simulated repair at room temperature after cooling to room temperature; C — stress evolution on the simulated repair at a preheat of 750°C immediately after the completion of the deposit; D — stress evolution on the simulated repair at 750°C after cooling to room temperature.

where γ_{SL} is the surface tension on a grain boundary containing a liquid film of thickness h. The value of γ_{SL} is approximately 0.307 J/m^2 (Ref. 42). Assuming a value of 10–15-nm-thick liquid film shows that the critical stress was approximately 6–8 MPa. Therefore, at the temperatures and stresses predicted by the simulations for the samples fabricated at RT, it is quite possible for cracking to occur in the deposits. However, the simulation showed that the stresses in the sample fabricated with a preheat of 750°C were predominantly compressive, and, therefore, one cannot expect grain boundary cracking.

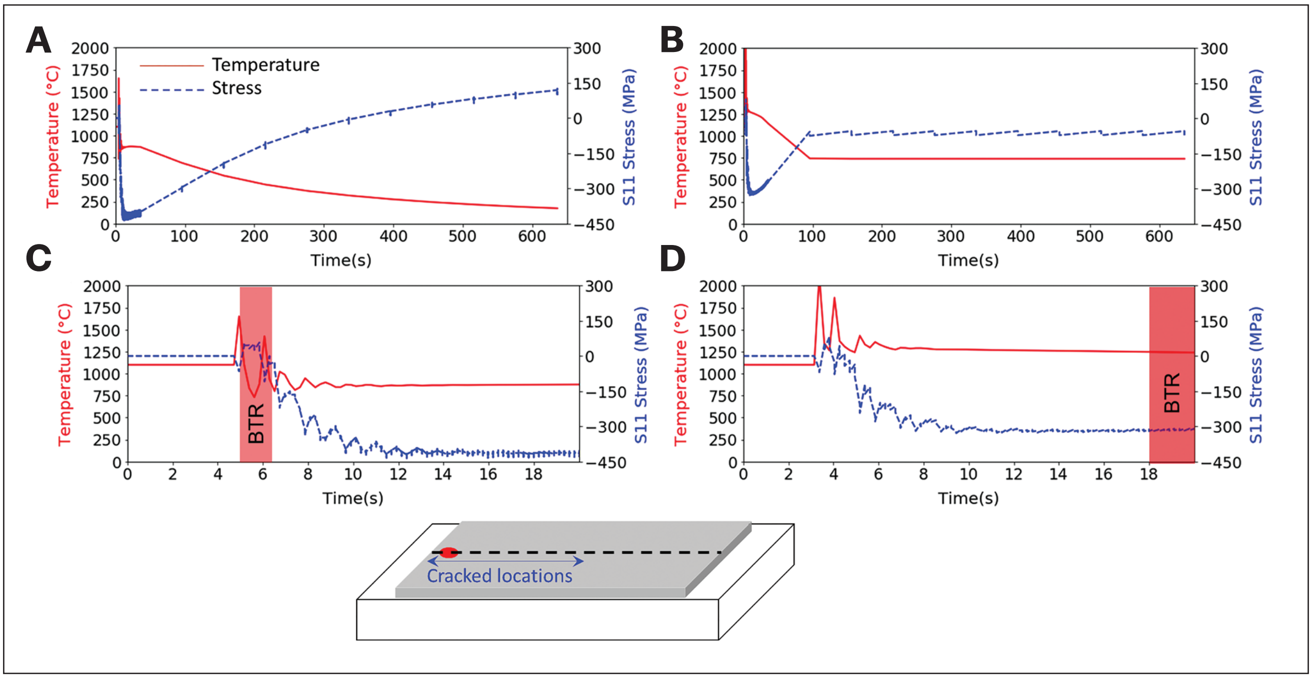

Fig. 10 — The temperature and stress evolution with respect to time: A–B — Stress evolution on the simulated repair without any preheat; C–D — stress evolution on the simulated repair at a preheat of 750°C. Both the locations are from the HAZ and correspond to the region identified with a red spot.

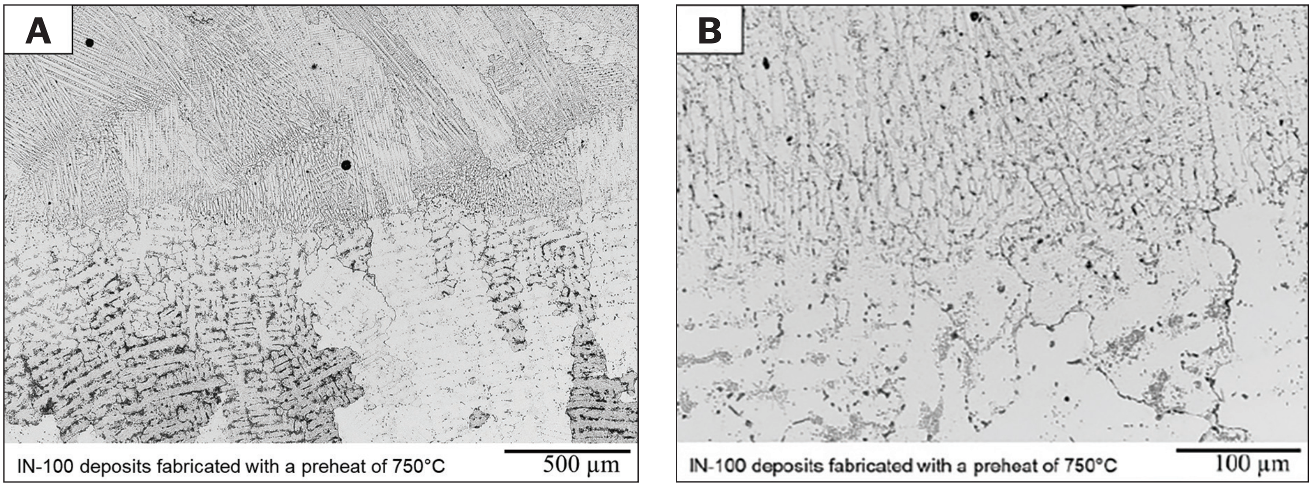

Fig. 11 — Optical micrographs of the simulated repair performed with a preheat of 750°C showing the absence of cracking: A — 100×; B — 200× showing the interface.

Deposits Fabricated with a Preheat Temperature

The micrographs of the preheated deposits are shown in Fig. 11. Figures 11A and B show the deposit substrate interface without any cracks. Figures 12A and B show the SEM micrographs of the same interface at higher magnification, showing that despite the presence of significant grain boundary carbide phases similar to the as-received material, cracking did not occur. This would have been due to compressive thermal stress, which could have suppressed the cracking of these liquating phases. Figure 12A shows the micrograph of the deposit. No γ' was observed in the deposit, however, the inset shows the deposit at higher magnification and the presence of carbides in the interdendritic region can be seen. However, no postrepair heat treatments were performed. Such heat treatments are also expected to demonstrate the repaired deposit's resistance to strain-age cracking during rejuvenation/postweld heat treatment of the repaired parts. Considering that this study has been able to demonstrate that multibead deposits with sizes and geometries are relevant to the airline repair industry, future studies should focus on the postprocessing of these deposits where

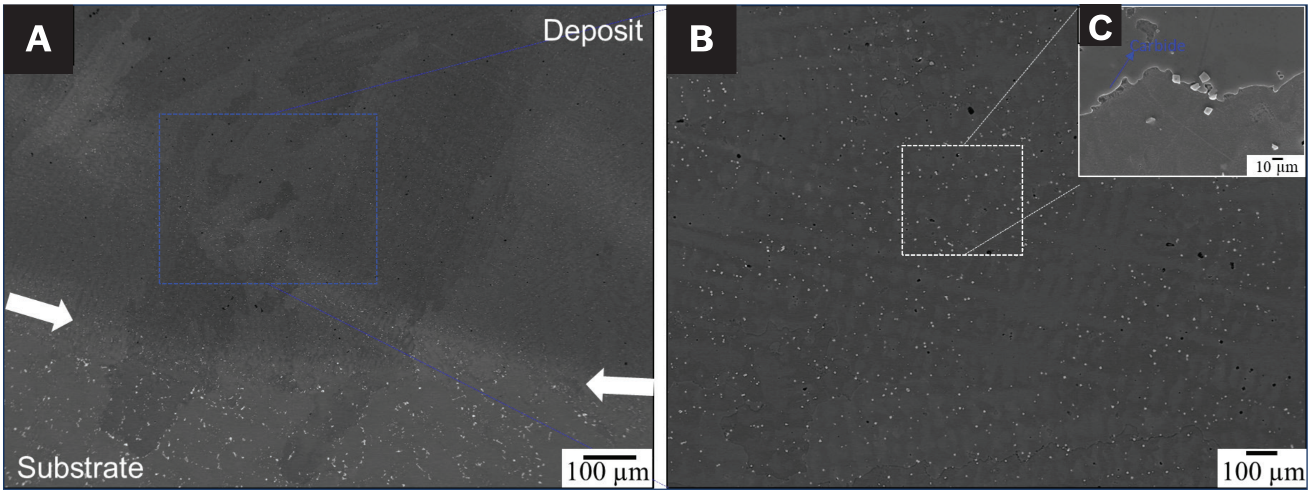

Fig. 12 — The SEM micrograph of the simulated repair performed with a preheat of 750°C showing the absence of cracking: A — The repaired deposit and the substrate; B — deposit at high magnification clearly showing the absence of γ′; C — inset showing the presence of grain boundary carbides probably formed at the final stages of solidification.

different rejuvenation treatments and the susceptibility to strain-age cracking can be explored.

Conclusions

Deposits were fabricated using a laser-directed energy deposition process on high γ′ Ni-based superalloy substrates in both as-cast and solution-annealed conditions. Severe cracking was observed in both cases. Detailed characterization showed two distinct mechanisms of crack formation. Cracks occurred primarily in the HAZ due to the partial liquation of the grain boundary carbides. Cracks in the deposits were predominantly solidification cracking. A parametric study of the process parameters indicated that cracking was minimized for the samples with high laser power, tighter hatch spacing, and high travel speed. Cracks occurred as a result of a synergistic effect of tensile stresses and liquating phases, and to effectively eliminate cracks, thermomechanical modeling was performed to optimize the preheat temperature. The cracking mechanisms were compared with cracking mechanisms described in other high γ′ alloys (IN-738 and MAR-M-247), and the operating mechanisms were consistent with observed cracking in literature. The modeling results showed that when the deposits were made with a preheat of 750°C, the stress was predominantly compressive, while those made without preheat temperature were tensile. Therefore, based on the modeling work, deposits were then fabricated on the as-cast substrate with a preheat temperature of 750°C. Characterization showed that the deposits were crack free, showing that the observed procedure can be effectively used for repairing high γ′ Ni alloy parts used in the hot section. Typically, all high γ′ alloys (γ′ fraction > 50%) have a distribution of carbides that could liquate during localized heating. The addition of solutes to promote γ′ precipitation also widens the solidification range of these alloys. Therefore, all high γ′ alloys are susceptible to the described cracking mechanisms, and the solution proposed could be applied to a much larger spectrum of alloys.

Acknowledgments

The authors would like to acknowledge the U.S. Department of Energy, Office of Energy Efficiency and Renewable Energy (EERE), Advanced Manufacturing Office Technical Collaborations program. This research was a result of the collaboration between Oak Ridge National Laboratory (ORNL) and Delta Tech Ops. This CRADA/NFE-17-06791 was conducted as a technical collaboration project within the ORNL Manufacturing Demonstration Facility (MDF) sponsored by the U.S. Department of Energy Advanced Manufacturing Office (CPS Agreement Number 24761). Opportunities for MDF technical collaborations are listed in the announcement "Manufacturing Demonstration Facility: Technology Collaborations for U.S. Manufacturers in Advanced Manufacturing and Materials Technologies" posted at *sam.gov/opp/eaf639a7ff90caae05bec2c5bbd44794/view*. The goal of technical collaborations is to engage industry partners to participate in short-term, collaborative projects within the MDF to assess the applicability of new energy-efficient manufacturing technologies. Research sponsored by the U.S. Department of Energy, EERE, Advanced Manufacturing Office, under contract DE-AC05-00OR22725 with UT-Battelle LLC. The authors would also like to acknowledge Tom Geer and Victoria Cox for preparing the samples for metallographic examination. On behalf of all authors, the corresponding author states that there is no conflict of interest.

these results of federally sponsored research in accordance with the DOE Public Access Plan (*energy.gov/doe-public-access-plan*).

References

1. Henderson, M. B., Arrell, D., Larsson, R., Heobel, M., and Marchant, G. 2004. Nickel based superalloy welding practices for industrial gas turbine applications. *Sci. Technol. Weld. Join.* 9(1): 13–21.

2. Sexton, L., Lavin, S., Byrne, G., and Kennedy, A. 2002. Laser cladding of aerospace materials. *J. Mater. Process. Technol.* DOI: 10.1016/S0924-0136(01)01121-9

3. Acharya, R., and Das, S. 2015. Additive manufacturing of IN100 superalloy through scanning laser epitaxy for turbine engine hot-section component repair: Process development, modeling, microstructural characterization, and process control. *Metall. Mater. Trans. A* 46(9): 3864–3875.

4. Egbewande, A. T., Buckson, R. A., and Ojo, O. A. 2010. Analysis of laser beam weldability of Inconel 738 superalloy. *Mater. Charact.* DOI: 10.1016/j.matchar.2010.02.016

5. Aina, J. O., Ojo, O. A., and Chaturvedi, M. C. 2019. Enhanced laser weldability of an aerospace superalloy by thermal treatment. *Sci. Technol. Weld. Join.* 24(3): 225–234. DOI: 10.1080/13621718.2018.1518767

6. Ojo, O. A., Richards, N. L., and Chaturvedi, M. C. 2004. Liquation of various phases in HAZ during welding of cast Inconel* 738LC. *Mater. Sci. Technol*. DOI: 10.1179/026708304225019948

7. Zhong, M., Sun, H., Liu, W., Zhu, X., and He, J. 2005. Boundary liquation and interface cracking characterization in laser deposition of Inconel 738 on directionally solidified Ni-based superalloy. *Scr. Mater*. DOI: 10.1016/j.scriptamat.2005.03.047

8. Siefert, J. A., Shingledecker, J. P., DuPont, J. N., and David, S. A. 2015. Weldability and weld performance of candidate nickel based superalloys for advanced ultrasupercritical fossil power plants: Part II: Weldability and cross-weld creep performance. *Sci. Technol. Weld. Join.* DOI: 10.1080/13621718.2016.1143708

9. Miller, W. A., and Chadwick, G. A. 1967. On the magnitude of the solid/liquid interfacial energy of pure metals and its relation to grain boundary melting. *Acta Metall.* 16: 607. DOI: 10.1016/0001-6160(67)90104-6

10. David, S. A., Siefert, J. A., DuPont, J. N., and Shingledecker, J. P. 2015. Weldability and weld performance of candidate nickel base superalloys for advanced ultrasupercritical fossil power plants: Part I: Fundamentals. *Sci. Technol. Weld. Join.* 20(7): 532–552.

11. Siefert, J. A., Shingledecker, J. P., DuPont, J. N., and David, S. A. 2016. Weldability and weld performance of candidate nickel based superalloys for advanced ultrasupercritical fossil power plants Part II: Weldability and cross-weld creep performance. *Sci. Technol. Weld. Join.* 21(5): 397–427. DOI: 10.1080/13621718.2016.1143708

12. Henderson, M. B., Arrell, D., Heobel, M., Larsson, R., and Marchant, G. 2004. Nickel-based superalloy welding practices for industrial gas turbine applications. *Sci. Technol. Weld. Join.* DOI: 10.1179/136217104225017099

13. Pepe, J. J., and Savage, W. F. 1970. The weld heat-affected zone of the 18Ni maraging steels. *Welding Journal* 49(12): 545-s to 553-s.

14. Tancret, F. 2007. Thermo-calc and dictra simulation of constitutional liquation of γ′ (γ′) during welding of Ni base superalloys. *Comput. Mater. Sci*. DOI: 10.1016/j.commatsci.2007.02.008

15. Lippold, J. C. 2005. Recent developments in weldability testing for advanced materials.

16. Harris, K., and Wahl, J. B. 2004. CM 939 Weldable® alloy. DOI: 10.1115/gt2004-53966

17. Wahl, J. B., and Harris, K. 2007. CM 939 Weldable® alloy update. DOI: 10.1115/GT2007-27239

18. Çam, G., and Koçak, M. 1998. Progress in joining of advanced materials. *Int. Mater. Rev.* DOI: 10.1179/imr.1998.43.1.1

19. Su, C. Y., Chou, C. P., Wu, B. C., and Lih, W. C. 1997. Plasma transferred arc repair welding of the nickel-base superalloy IN-738LC. *J. Mater. Eng. Perform.* 6(5): 619–627. DOI: 10.1007/s11665-997-0055-7

20. Arjakine, N., Grüger, B., Bruck, J., Seeger, D. M., and Wilkenhoener, R. 2008. Advanced weld repair of gas turbine hot section components. DOI: 10.1115/GT2008-51534

21. McGraw, J., Van Deventer, G., Anton, R., and Burns, A. 2006. Advancements in gas turbine vane repair. DOI: 10.1115/POWER2006-88233

22. Dye, D., Hunziker, O., and Reed, R. C. 2001. Numerical analysis of the weldability of superalloys. *Acta Mater.* DOI: 10.1016/S1359-6454(00)00361-X

23. Frederick, G., Gandy, D., and Stover, J. T. 2002. Laser weld repair of service exposed IN738 and GTD 111 buckets. DOI: 10.1115/GT2002-30160

24. Bi, G., and Gasser, A. 2011. Restoration of nickel-base turbine blade knife-edges with controlled laser aided additive manufacturing. DOI: 10.1016/j.phpro.2011.03.051

25. Bi, G., Sun, C. N., Chi Chen, H., Ng, F. L., and Ma, C. C. K. 2014. Microstructure and tensile properties of superalloy IN100 fabricated by micro-laser aided additive manufacturing. *Mater. Des.* DOI: 10.1016/j.matdes.2014.04.020

26. Sridharan, N. et al. 2017. Design, fabrication, and characterization of graded transition joints. *Welding Journal* 96(8): 295-s to 306-s.

27. Cakmak, E. et al. 2018. Feasibility study of making metallic hybrid materials using additive manufacturing. *Metall. Mater. Trans. A Phys. Metall. Mater. Sci*. (49): 5035–5041. DOI: 10.1007/s11661-018-4741-x

28. Chiang, M. F., and Chen, C. 2009. Induction-assisted laser welding of IN-738 nickel-base superalloy. *Mater. Chem. Phys*. DOI: 10.1016/j.matchemphys.2008.09.051

29. Xu, J. et al. 2017. The effect of preheating on microstructure and mechanical properties of laser solid forming IN-738LC alloy. *Mater. Sci. Eng. A* 691(3): 71–80. DOI: 10.1016/j.msea.2017.03.046

30. Goldak, J., Chakravarti, A., and Bibby, M. 1984. A new finite element model for welding heat sources. *Metall. Trans. B.* DOI: 10.1007/BF02667333

31. Pollock, T. M., and Tin, S. 2006. 102 Nickel-based superalloys for advanced turbine engines chemistry, microstructure, and properties. *J. Propuls. Power* 22(2): 361–374.

32. Wusatowska-Sarnek, A. M., Ghosh, G., Olson, G. B., Blackburn, M. J., and Aindow, M. 2003. Characterization of the microstructure and phase equilibria calculations for the powder metallurgy superalloy IN100. *J. Mater. Res.* DOI: 10.1557/JMR.2003.0371

33. Kozar, R. W., Suzuki, A., Milligan, W. W., Schirra, J. J., Savage, M. F., and Pollock, T. M. 2009. Strengthening mechanisms in poly-

crystalline multimodal nickel-base superalloys. *Metall. Mater. Trans. A Phys. Metall. Mater. Sci.* 40(7): 1588–1603. DOI: 10.1007/s11661-009-9858-5

34. Collins, M. G., Ramirez, A. J., and Lippold, J. C. 2004. An investigation of ductility-dip cracking in nickel-based weld metals — Part III. *Welding Journal* 83(2): 39-s to 49-s.

35. Collins, M. G., Ramirez, A. J., and Lippold, J. C. 2003. An investigation of ductility dip cracking in nickel-based weld metals — Part II. *Welding Journal* 82(12): 348-s to 354-s.

36. Lee, Y. S. et al. 2018. Asymmetric cracking in Mar-M247 alloy builds during electron beam powder bed fusion additive manufacturing. *Metall. Mater. Trans. A Phys. Metall. Mater. Sci.* DOI: 10.1007/s11661-018-4788-8

37. Ojo, O. A., Richards, N. L., and Chaturvedi, M. C. 2004. Contribution of constitutional liquation of γ' precipitate to weld HAZ cracking of cast Inconel 738 superalloy. *Scr. Mater.* DOI: 10.1016/j.scriptamat.2003.11.025

38. Ojo, O. A., Richards, N. L., and Chaturvedi, M. C. 2004. Microstructural study of weld fusion zone of TIG welded IN 738LC nickel-based superalloy. *Scr. Mater.* DOI: 10.1016/j.scriptamat.2004.06.013

39. Gasko, K. L., Janowski, G. M., and Pletka, B. J. 1988. The influence of eutectic on the mechanical properties of conventionally cast MAR-M 247. *Mater. Sci. Eng.* A 104: 1–8.

40. Waly, M., and Nofal, A. 2008. Effect of various heat treatment conditions on microstructure of cast polycrystalline IN738LC alloy. *Mater. Sci. Eng. A* 487: 152–161. DOI: 10.1016/j.msea.2007.10.004

41. Rush, M. T., Colegrove, P. A., Zhang, Z., and Broad, D. 2012. Liquation and post-weld heat treatment cracking in Rene 80 laser repair welds. *J. Mater. Process. Technol.* 212(1): 188–197. DOI: 10.1016/j.jmatprotec.2011.09.001

42. Wang, N., Mokadem, S., Rappaz, M., and Kurz, W. 2004. Solidification cracking of superalloy single- and bi-crystals. *Acta Mater.* 52: 3173–3182. DOI: 10.1016/j.actamat.2004.03.047

43. Ojo, O. A., Chaturvedi, M. C., and Society, M. 2007. Liquation microfissuring in the weld heat-affected zone of an overaged precipitation-hardened nickel-base superalloy. *Metall. Mater. Trans. A* 38A: 356–369. DOI: 10.1007/s11661-006-9025-1

44. DuPont, J. N., Lippold, J. C., and Kiser, S. D. 2009. *Welding Metallurgy and Weldability of Nickel-Base Alloys*. New Jersey: John Wiley & Sons.

45. Lin, W. A. B. I., and Lippold, J. C. 1993. An evaluation of heat-affected zone liquation cracking susceptibility, Part I: Development of a method for quantification. *Welding Journal* 72(4): 135-s to 153-s.

46. Xu, J. et al. 2018. The initiation and propagation mechanism of the overlapping zone cracking during laser solid forming of IN-738LC superalloy. *J. Alloys Compd.* 749: 859–870. DOI: 10.1016/j.jallcom.2018.03.366

47. Danis, Y., Arvieu, C., Lacoste, E., Larrouy, T., and Quenisset, J. M. 2010. An investigation on thermal, metallurgical and mechanical states in weld cracking of Inconel 738LC superalloy. *Mater. Des.* 31: 402–416. DOI: 10.1016/j.matdes.2009.05.041

48. Miller, W. A., and Chadwick, G. A.1967. On the magnitude of the solid/liquid interfacial energy of pure metals and its relation to grain boundary melting. *Acta Metall.* 16: 607. DOI: 10.1016/0001-6160(67)90104-6

NIYANTH SRIDHARAN (*niyanth.sridharan@gmail.com*) is with the Material Science and Technology Divison, Oak Ridge National Laboratory, Oak Ridge, Tenn., and The Lincoln Electric Co., Chengalpattu, Tamil Nadu, India. **YOUSUB LEE** is with the Computational Sciences and Engineering Division, Oak Ridge National Laboratory, Oak Ridge, Tenn. **BRIAN JORDAN** is with the Material Science and Technology Divison, Oak Ridge National Laboratory, Oak Ridge, Tenn. **JOHN ROBERTSON** and **RAMESH RAMAKRISHNAN** are with Delta Airlines TechOps, Atlanta, Ga.